Acoustic spin-1 Weyl semimetal

WeiYin Deng[1†], XueQin Huang[1†], JiuYang Lu[1], Feng Li[1*], JiaHong Ma[1],
ShuQi Chen[3*], and ZhengYou Liu[2,4*]

[1] *School of Physics and Optoelectronics, South China University of Technology, Guangzhou 510640, China;*
[2] *Key Laboratory of Artificial Micro- and Nanostructures of Ministry of Education, School of Physics and Technology,*
Wuhan University, Wuhan 430072, China;
[3] *Key Laboratory of Weak Light Nonlinear Photonics of Ministry of Education, School of Physics,*
Nankai University, Tianjin 300071, China;
[4] *Institute for Advanced Studies, Wuhan University, Wuhan 430072, China*

The study of topological semimetals hosting spin-1 Weyl points (WPs) beyond Dirac points and WPs has attracted a great deal of attention. However, a spin-1 Weyl semimetal that exclusively possesses spin-1 WPs in a clean frequency window without being shadowed by any other nodal points is yet to be discovered. This study reports a spin-1 Weyl semimetal in a phononic crystal. Its spin-1 WPs are touched by two linear dispersions and an additional flat band and carry monopole charges $(-2,0,2)$ or $(2,0,-2)$ for the three bands from the bottom to the top. They result in double Fermi arcs, which occur between the first and second bands, as well as between the second and third bands. Further robust propagation is observed against the multiple joints and topological negative refraction of the acoustic surface arc wave. The results of this study create the basis for the exploration of the unusual properties of spin-1 Weyl physics on a macroscopic scale.

spin-1 Weyl point, phononic crystal, topological surface states

PACS number(s): 43.40.+s, 63.20.–e, 03.65.Vf

1 Introduction

The discovery of Dirac and Weyl semimetals [1-8] featuring fourfold and twofold linear crossing points in their band structures has opened up a new field of research known as topological semimetals [9,10]. The low-energy excitations near the Dirac points and Weyl points (WPs) are described by the Dirac and Weyl equations; thus, they behave like Dirac and Weyl fermions, i.e., the relativistic spin-1/2 fermions in quantum field theory. Unlike the fermions in high-energy theories, the excitations in crystals are protected by the rich symmetries of the space group (rather than the Poincaré symmetry) and give rise to new physical phenomena, such as type-II Weyl semimetals [11], nodal line semimetals [12], and spin-1 Weyl semimetals [13]. The spin-1 Weyl semimetals, which exclusively host spin-1 WPs in a frequency window without being shadowed by any other nodal points, have recently been proposed in electronic and cold atom materials [13-15]. However, the spin-1 Weyl semimetal is yet to be realized.

Spin-1 WPs are threefold degenerate points that are tou-

ched by two linear dispersions and an additional flat band; furthermore, they also carry topological charges (−2,0,2) or (2,0,−2) [13]. Many interesting properties result from spin-1 WPs with nontrivial topology or chirality, such as double Fermi arcs [13,14], chiral anomaly [13], the quantized circular photogalvanic effect [16-18], chiral optical response [18,19], and novel Imbert-Fedorov shift [20]. In terms of theoretical predictions [16,21-24] and experimental observations [25-31], spin-1 WP coexisting with other chiral multifold points has been the focus of significant interest. Although spin-1 WPs have been reported in refs. [25-31], the topological charges of spin-1 WPs have not been completely verified. Only the topological charge −2 of the first band of spin-1 WP can be determined by double Fermi arcs. To explore the topological physics of spin-1 WP, it is necessary to realize a real spin-1 Weyl semimetal with pure spin-1 WPs.

This study presents the realization of a spin-1 Weyl semimetal in a three-dimensional (3D) phononic crystal (PC). The unique advantage of PCs over electronic materials lies in their macroscopic scale and the flexibility of fabrication. In this study's design, as there are only two spin-1 WPs near a frequency surface, the separation between the WPs can be sufficiently wide. This is so that the WPs and the associated surface arcs, which are similar to the Fermi arcs found in electronic systems, can be easily accessed in experiments. First, the study examines the spin-1 WPs in a layer-stacking Lieb lattice and reveals the phase diagram and topologically protected surface states. Then, a 3D PC corresponding to this lattice model is designed, and the experimental observations of the spin-1 WPs and surface arcs are presented. The theoretical and experimental results are found to be in good agreement.

2   Methodology of simulations and experiments

PC full-wave simulations were performed using the commercial COMSOL Multiphysics solver package. The systems were filled with air at a mass density of $\rho=1.18$ kg m^{-3} and a sound velocity of $v=346$ m s^{-1} at room temperature. Because of the huge mismatch of acoustic impedance compared with air, during the simulations, the plastic stereolithographics were considered as rigid boundaries. The periodic boundary conditions were applied in all three directions of a unit cell to calculate the bulk dispersions; rigid boundaries were applied in the x-direction, and periodic boundaries were applied in the y- and z-directions of a ribbon structure to calculate the surface-state dispersions.

For the experimental measurements, the sample was stacked with 23 layers along the z-direction with each layer containing 26×26-unit cells. Acoustic excitation was achieved using a sub-wavelength headphone with a 3.0-mm diameter. This was placed at the center of the 3D sample for bulk state excitations and at the center of the corresponding surface with rigid boundaries for surface wave excitations. A sub-wavelength microphone probe with a 1.5-mm diameter was used to measure the acoustic pressure fields in the samples. A Keysight 5061B network analyzer was used to send and receive the acoustic signals. The pressure fields were measured inside the sample and were Fourier transformed into the reciprocal space to obtain the plane wave components of the excited Bloch states in all the Brillouin zones (BZs). The Bloch states were constructed by picking up and assembling the corresponding plane wave components in all BZs. The bulk band structure was then expressed in terms of Bloch states by calculating and plotting the average intensity of the wave function over a unit cell in the first BZ for all states.

3   Results and discussion

3.1   Tight-binding model

To effectively illustrate the development of spin-1 WPs, this study constructed a tight-binding model based on a layer-stacking Lieb lattice with a three-site unit cell, which is denoted by A (red sphere), B (yellow sphere), and C (blue sphere) in the upper panel of Figure 1(a). The nearest-neighbor hoppings of the intralayer in the xy plane are t_0, and the interlayer couplings (dashed lines) are chiral with strength t_z. Based on the sublattices (A–C), the Bloch Hamiltonian of this model can be described by

$$H = \begin{pmatrix} 0 & 2t_0\cos(k_xa/2) & 2t_0\cos(k_ya/2) \\ 2t_0\cos(k_xa/2) & 0 & t_{z1}\cos(k_zh)-it_{z2}\sin(k_zh) \\ 2t_0\cos(k_ya/2) & t_{z1}\cos(k_zh)+it_{z2}\sin(k_zh) & 0 \end{pmatrix}, \tag{1}$$

where $t_{z1}=4t_z\cos(k_xa/2)\cos(k_ya/2)$, $t_{z2}=4t_z\sin(k_xa/2)\sin(k_ya/2)$, and t_0, $t_z<0$. The lattice constants in the x- (or y-) and z-directions are denoted by a and h, respectively. Diagonalizing the Hamiltonian (1) yields a pair of spin-1 WPs with zero energy located at points $M=(\pi/a, \pi/a, 0)$ and $R=(\pi/a, \pi/a, \pi/a)$

in the first BZ, as shown by the green and purple spheres in the left panel of Figure 1(b). These two spin-1 WPs at the M and R points are determined by three coexisting chiral symmetries along three mutually orthogonal lines (Supporting Material I). The threefold degenerate point consists
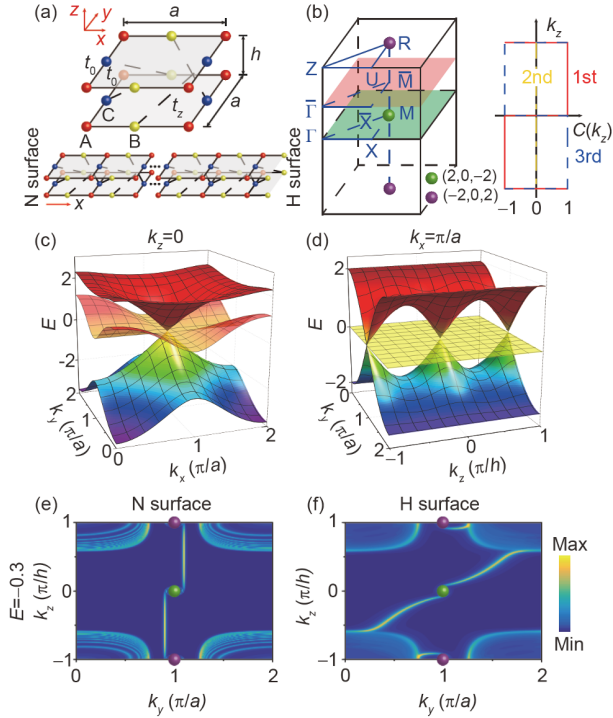
Figure 1 (Color online) Bulk band structures and surface arcs of the spin-1 WPs for the lattice model. (a) Schematic of the unit cell and ribbon. Upper panel: red, yellow, and blue spheres denote A, B, and C lattices in a unit cell. Lower panel: ribbon for calculating the surface-state dispersions. Two different opposite surfaces are marked as N and H surfaces, respectively. (b) Left panel: the first BZ of the system. The green and purple spheres represent spin-1 WPs with topological charges $(2,0,-2)$ and $(-2,0,2)$, respectively. Right panel: the Chern numbers of the three bands as a function of k_z. (c), (d) The 3D bulk band structures with $k_z=0$ and $k_x=\pi/a$. (e), (f) The surface arcs between the first and second bands for $E=-0.3$ on the N and H surfaces, respectively. The coupling parameters are taken to $t_0=-1$ and $t_z=-0.3$.

of two linear dispersions and an additional flat band in all momentum directions, as revealed in Figure 1(c) and (d). To explore the underlying physics of the threefold degenerate points, their low-energy effective excitations were developed to reveal their possession of the form $\mathbf{k}\cdot\mathbf{S}$, where $\mathbf{S}$ is the vector of the spin-1 matrix representing the sub-lattice pseudospin, as described in Supporting Material II. These threefold degenerate points are spin-1 WPs, since they are spin-1 generalizations of WPs. The emergence of spin-1 WPs can be interpreted as follows: the single layer, as a Lieb lattice, can support a two-dimensional (2D) threefold degenerate point at $(k_x, k_y)=(\pi/a, \pi/a)$ with a Hamiltonian in the form of $k_x S_x + k_y S_y$; meanwhile, the chiral interlayer coupling contributes to the third term of the Hamiltonian $k_z S_z$ near $k_z=0$ or π/h to generate the spin-1 WPs.

Next, the topological properties of the system were studied. The monopole charges of the spin-1 WPs were calculated to obtain $C_M=(2,0,-2)$ and $C_R=(-2,0, 2)$ (Supporting Material III). The spin-1 WPs behave as monopoles of the Berry flux in momentum space, which are twice those of the WPs with spin-1/2. By considering k_z as a parameter, the

Chern numbers $C(k_z)$ of the three bands were plotted in the right panel of Figure 1(b). Supporting Material IV contains a more complete phase diagram. The monopole charges of the spin-1 WPs are consistent with the k_z-dependent Chern numbers $C(k_z)$; for instance, the charge for the first band at M is $C(k_z=0^+)-C(k_z=0^-)=2$. In this study's structure, there are two types of surfaces corresponding to two different surface cuts, as illustrated by the right and left sides of the bottom panel in Figure 1(a). The hollow (H) surface is one of those; its termination has a hollow concave, while the normal (N) surface has a normal flat termination. After selecting the open boundaries in the x-direction, the surface arcs between the first and second bands on the N and H surfaces were plotted, as shown in Figure 1(e) and (f), respectively. Because of the C_4 symmetry, the dispersions on the ZX surface are the same as the above results on the YZ surface. Two surface arcs connect the projections of two oppositely charged spin-1 WPs, coexisting with the bulk states of the second band near the spin-1 WPs. The surface arcs between the second and third bands and the surface-state dispersions are displayed in Supporting Material V. The double surface arcs, which both exist between the first and second bands and between the second and third bands, provide solid evidence for the topological charges of the spin-1 WPs. An illustration of the surface arcs of the spin-1 WPs is contained in Supporting Material VI.

3.2   Acoustic spin-1 Weyl points

Next is a consideration of a real PC for realizing the spin-1 Weyl semimetal for acoustic waves. As Figure 2(a) reveals, the PC sample is a layer-stacking structure fabricated by 3D printing. The unit cell, shown in Figure 2(b), contains three tube-linked non-equivalent cavities; the gray areas represent rigid boundaries, and the green areas denote periodic boundaries. The cavities can be generally viewed as the lattice sites, while the tubes provide the hopping parameters. The intralayer tubes are set to be the same size to produce equal couplings in the xy plane, which corresponds to the Lieb lattice. The interlayer tubes are chiral to connect the different cavities, which induces an effective gauge flux [7].

The structure possesses the $P4$ (No. 75) and time-reversal symmetries, which do not have 3D irreducible representations at the high symmetry points. Therefore, the induction of the spin-1 WPs is only possible by the accidental degeneration of one-dimensional and 2D irreducible representations at both M and R. The size l_2 of one cavity is adjusted and different to the size l_1 of the other cavities (Supporting Material VII). At M, if l_2 is smaller than 3 mm, the frequency of the double-degenerate state is higher than that of the single state; if l_2 is larger than 3 mm, the frequency of the double-degenerate state is lower than that of the single state. The band inversion of the single state and the double degenerate
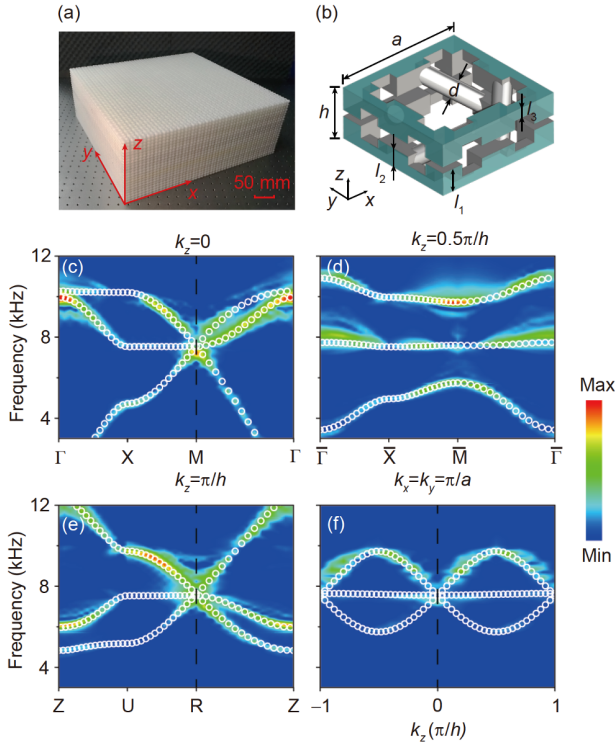
Figure 2 (Color online) Experimental demonstration of the bulk band structures of the spin-1 WPs in the PC. (a) Photos of the 3D sample and (b) unit cell of the PC. Here, a=20 mm, h=8 mm, l_1=3.5 mm, l_2=3 mm, l_3=1.6 mm, and d=2.72 mm. The periodic boundaries are applied in the x-, y-, and z-directions. The gray areas represent hard boundaries. (c)-(f) The bulk band structures of the three lowest modes in k_z=0, k_z=0.5π/h, k_z=π/h and along the k_z direction. The color maps represent the experimental data, and the white circles represent the full-wave simulation results.

state with different l_2 guarantee the existence of a threefold degenerate state for l_2=3 mm. Essentially, spin-1 WPs are easily generated by accidental degeneracy in real PCs since the acoustic sample is closely a one-to-one mapping of the tight-binding model in which cavities map to atoms and tubes map to bonds. The existence of spin-1 WPs guarantees the uniformity of the Hamiltonian's on-site energies. Therefore, the real PC can be well modeled by the tight-binding Hamiltonian (Supporting Material VIII).

To confirm the existence of the pair of acoustic spin-1 WPs illustrated in Figure 1(b), the 2D band structures for fixed k_z=0 and k_z=π/h were calculated and measured, as shown in Figures 2(c) and (e), respectively. The color maps represent the experimental dispersions expressed in terms of the average intensity of the Bloch states, while the white circles represent the simulated values obtained from full-wave simulations (see Methodology of simulations and experiments). Threefold degenerate points at the M and R points are clearly observed at approximately the same frequency of 7.5 kHz. In Figure 2(c), multiple reflections by the surfaces of the finite sample may cause the finer structure near the Γ point below the second band. In Figure 2(d), the dispersion on the plane k_z=0.5π/h opens two gaps between the three

bands at the $\overline{\text{M}}$ point due to effective time-reversal symmetry breaking by the synthetic gauge flux. The simulated and experimental results for the band dispersions along the k_z direction are shown in Figure 2(f), which correspond to the band structure in Figure 1(d). It is evident that the dispersions near the threefold degenerate points are the crossings of two linear bands and an additional flat band. This clearly indicates that the two threefold degenerate points are spin-1 WPs in the 3D band structure.

3.3 Acoustic surface arc waves

Theoretical studies predict that the non-zero Chern numbers $C(k_z)$ can lead to a pair of gapless surface states for a ribbon structure. Experimentally, surface-state dispersions can be obtained by measuring and Fourier transforming the surface acoustic fields, which are shown in Supporting Material IX. Given that k_z=0.5π/h, the surface-state dispersions along the k_y direction are plotted in Figure 3(a) and (b) for the N and H surfaces, respectively. Surface-state dispersions are observed between the first and second bands and between the second and third bands, which result from the same topology for $C(k_z)$=0 of the second band. Compared with the dispersions of surface state in the tight-binding model, it is evident that the PC results are consistent with the tight-binding model.
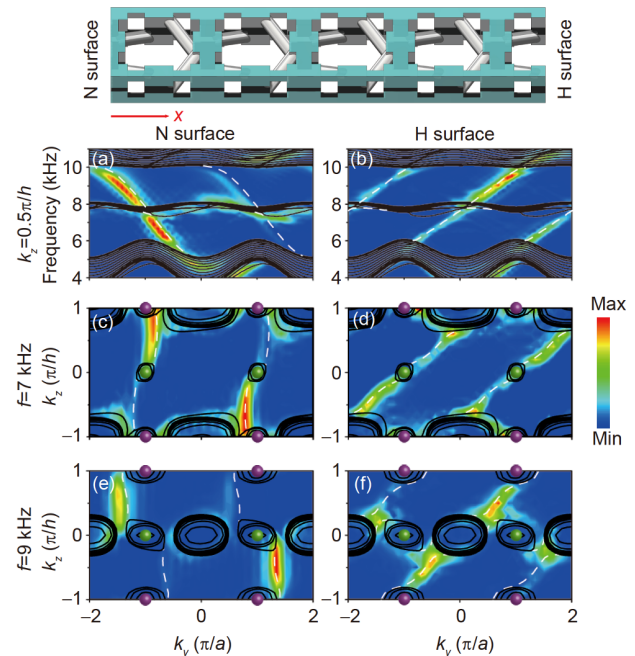

Figure 3 (Color online) Surface-state dispersions and acoustic surface arcs. The top image is a schematic of the ribbon for full-wave simulations of surface-state dispersions and surface arcs. (a), (b) The dispersions of the surface state with fixed k_z=0.5π/h on the N and H surfaces. (c)-(f) The equifrequency contours of the surface state at fixed frequencies of f=7 kHz and f=9 kHz on the N and H surfaces, respectively. The color maps denote the experimental data, and the white dashed and black lines represent the calculated dispersions of the surface state and projected bulk state, respectively.

For a given excitation frequency, the surface states in the PC will mark out trajectories to connect the two oppositely charged spin-1 WPs and form surface arcs. The surface arcs between the first and second bands on the N and H surfaces at f=7 kHz are shown in Figure 3(c) and (d), respectively. The surface arcs connecting the pair of spin-1 WPs exhibit two branches and exist in $k_z \in (0, \pi/h)$ and $k_z \in (-\pi/h, 0)$. Additionally, the surface arcs near the spin-1 WPs merge with the projections of the bulk states, which is consistent with the theoretical results presented in Figure 1(e) and (f). Similar features of surface arcs at f=9 kHz are also observed between the second and third bands, as shown in Figure 3(e) and (f). The topological charges of the spin-1 WPs were wholly verified by the double surface arcs observed between the first and second bands and between the second and third bands. Of note are the rigid wall boundary conditions in the simulations and experiments. Tuning the distance between the sample and wall alters the configurations of the surface dispersions and the Fermi arcs. However, the surface states must connect the bulk bands and be gapless in the bulk gaps, which are guaranteed by the k_z-dependent Chern numbers. Correspondingly, the double Fermi arcs should both exist between the first and second bands and between the second and third bands, connecting the pair of spin-1 WPs.

3.4   Topological reflection-free propagations

Surface arcs with a non-closed nature can produce intriguing topological phenomena, including anomalous quantum oscillations [32,33], the 3D quantum Hall effect [34,35], and topological negative refraction [36]. Figure 4 presents two experiments visualizing unusual topological reflection-free propagations of surface arc waves. The first experiment demonstrates the robust propagation of the surface arc wave against the multiple joints of adjacent facets, as shown in Figure 4(a) and (b). The second investigation displays the topological negative refraction, as shown in Figure 4(c)-(e). This phenomenon has also been observed in 2D valley Hall insulators [37,38]. It is evident that the propagation of the surface arc waves along the boundary only occurs in an anticlockwise manner; they do not reflect or scatter due to the configuration of the non-closed surface arc (Figure 4(d)). The measured fields in Figure 4(b) and (e) resemble the interference pattern result from the field variation in a unit cell rather than the interference between the incident and reflection waves. It is worth highlighting that these topological propagations can occur at the frequencies not only between the first and second bands but also between the second and third bands, as shown in Supporting Material X. The attenuations of the surface arc waves during propagation due to the absorption of air and the decaying behaviors of the surface arc waves along the perpendicular direction are shown in Supporting Material XI.
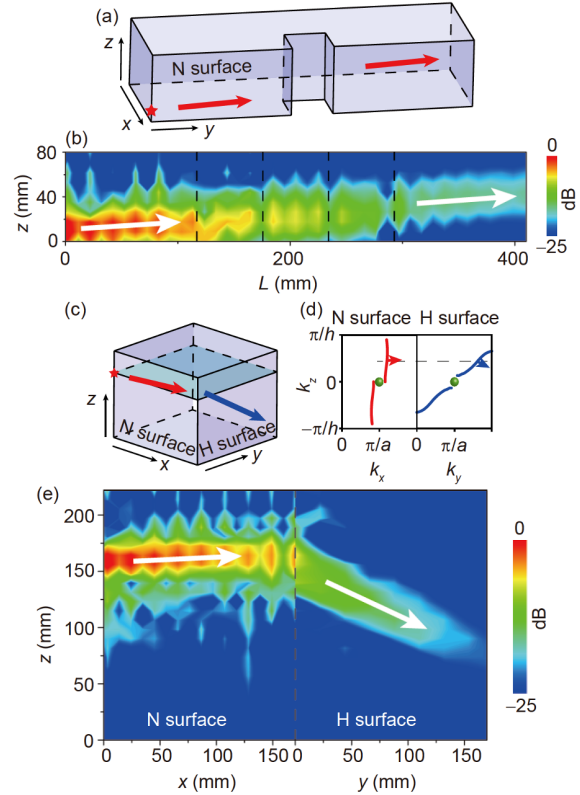

Figure 4   (Color online) Experimental topological reflection-free propagations of acoustic surface arc waves. (a) Schematic of a sample with the multiple joints of adjacent facets on the N surface. (b) Experimental robust propagation of the surface arc wave through the multiple joints of adjacent facets. (c) Schematic of the topological negative refraction at the interface between the N and H surfaces. (d) Group velocities (red and blue arrows) of the surface arc waves of the N and H surfaces. The non-closed properties of the surface arcs guarantee reflection immunity. (e) Experimental observation of topological negative refraction. In both wave propagation experiments, the field distributions were measured at a frequency of f=7 kHz. The red stars denote the position of excitation, and the arrows represent the directions of propagation.

4   Conclusions

This study realized an acoustic spin-1 Weyl semimetal, which creates the basis for the exploration of new topological physics in acoustics [7,8,36-42] besides spin-1/2 Weyl semimetals. Unlike the acoustic system that hosts a spin-1 WP coexisting with a fourfold point [30], the structure in this study possesses the pure spin-1 WPs. This is referred to as a real spin-1 Weyl semimetal, in which the topological charges are completely demonstrated. Therefore, this study's system is crucial for exploring the topological properties of spin-1 WPs, including the surface arc states and chiral anomaly [13]. The robust propagation against the multiple joints of adjacent facets and topological negative refraction of surface arc waves may offer a basis for designing innovative acoustic devices. The flat bands of spin-1 WPs may be used to localize or freeze acoustic waves [43-45] and enhance local fields [46-48] because of their slow group velocities and high densities of state. Moreover, the layer-stacking method in

this study can extend to other periodic structures, including electronic, photonic, and cold atom systems. Finally, in this spin-1 Weyl semimetal, the chiral Landau levels induced by a pseudo-magnetic field are of significant interest and can be implemented via inhomogeneous potentials [42].

Supporting Information

The supporting information is available online at phys.scichina.com and http://link.springer.com/journal/11433. The supporting materials are published as submitted, without typesetting or editing. The responsibility for scientific accuracy and content remains entirely with the authors.

1 X. Wan, A. M. Turner, A. Vishwanath, and S. Y. Savrasov, Phys. Rev. B **83**, 205101 (2011).
2 Z. Wang, Y. Sun, X. Q. Chen, C. Franchini, G. Xu, H. Weng, X. Dai, and Z. Fang, Phys. Rev. B **85**, 195320 (2012).
3 Z. K. Liu, B. Zhou, Y. Zhang, Z. J. Wang, H. M. Weng, D. Prabhakaran, S. K. Mo, Z. X. Shen, Z. Fang, X. Dai, Z. Hussain, and Y. L. Chen, Science **343**, 864 (2014).
4 B. Q. Lv, H. M. Weng, B. B. Fu, X. P. Wang, H. Miao, J. Ma, P. Richard, X. C. Huang, L. X. Zhao, G. F. Chen, Z. Fang, X. Dai, T. Qian, and H. Ding, Phys. Rev. X **5**, 031013 (2015).
5 S. Y. Xu, I. Belopolski, N. Alidoust, M. Neupane, G. Bian, C. Zhang, R. Sankar, G. Chang, Z. Yuan, C. C. Lee, S. M. Huang, H. Zheng, J. Ma, D. S. Sanchez, B. K. Wang, A. Bansil, F. Chou, P. P. Shibayev, H. Lin, S. Jia, and M. Z. Hasan, Science **349**, 613 (2015).
6 L. Lu, Z. Wang, D. Ye, L. Ran, L. Fu, J. D. Joannopoulos, and M. Soljačić, Science **349**, 622 (2015).
7 M. Xiao, W. J. Chen, W. Y. He, and C. T. Chan, Nat. Phys. **11**, 920 (2015).
8 F. Li, X. Huang, J. Lu, J. Ma, and Z. Liu, Nat. Phys. **14**, 30 (2018).
9 A. A. Burkov, Nat. Mater. **15**, 1145 (2016).
10 N. P. Armitage, E. J. Mele, and A. Vishwanath, Rev. Mod. Phys. **90**, 015001 (2018).
11 A. A. Soluyanov, D. Gresch, Z. Wang, Q. S. Wu, M. Troyer, X. Dai, and B. A. Bernevig, Nature **527**, 495 (2015).
12 A. A. Burkov, M. D. Hook, and L. Balents, Phys. Rev. B **84**, 235126 (2011).
13 B. Bradlyn, J. Cano, Z. Wang, M. G. Vergniory, C. Felser, R. J. Cava, and B. A. Bernevig, Science **353**, aaf5037 (2016).
14 Y. Q. Zhu, D. W. Zhang, H. Yan, D. Y. Xing, and S. L. Zhu, Phys. Rev. A **96**, 033634 (2017).
15 I. C. Fulga, L. Fallani, and M. Burrello, Phys. Rev. B **97**, 121402 (2018).
16 G. Chang, S. Y. Xu, B. J. Wieder, D. S. Sanchez, S. M. Huang, I. Belopolski, T. R. Chang, S. Zhang, A. Bansil, H. Lin, and M. Z. Hasan, Phys. Rev. Lett. **119**, 206401 (2017).
17 D. Rees, K. Manna, B. Lu, T. Morimoto, H. Borrmann, C. Felser, J. E. Moore, D. H. Torchinsky, and J. Orenstein, arXiv: 1902.03230.
18 F. Flicker, F. de Juan, B. Bradlyn, T. Morimoto, M. G. Vergniory, and A. G. Grushin, Phys. Rev. B **98**, 155145 (2018).
19 M. Á. Sánchez-Martínez, F. de Juan, and A. G. Grushin, Phys. Rev. B **99**, 155145 (2019).
20 Y. R. Hao, L. Wang, and D. X. Yao, Phys. Rev. B **99**, 165406 (2019).
21 J. L. Mañes, Phys. Rev. B **85**, 155118 (2012).
22 P. Tang, Q. Zhou, and S. C. Zhang, Phys. Rev. Lett. **119**, 206402 (2017).
23 M. Saba, J. M. Hamm, J. J. Baumberg, and O. Hess, Phys. Rev. Lett. **119**, 227401 (2017).
24 T. Zhang, Z. Song, A. Alexandradinata, H. Weng, C. Fang, L. Lu, and Z. Fang, Phys. Rev. Lett. **120**, 016401 (2018).
25 S. Bao, J. Wang, W. Wang, Z. Cai, S. Li, Z. Ma, D. Wang, K. Ran, Z. Y. Dong, D. L. Abernathy, S. L. Yu, X. Wan, J. X. Li, and J. Wen, Nat. Commun. **9**, 2591 (2018).
26 H. Miao, T. T. Zhang, L. Wang, D. Meyers, A. H. Said, Y. L. Wang, Y. G. Shi, H. M. Weng, Z. Fang, and M. P. M. Dean, Phys. Rev. Lett. **121**, 035302 (2018).
27 D. Takane, Z. Wang, S. Souma, K. Nakayama, T. Nakamura, H. Oinuma, Y. Nakata, H. Iwasawa, C. Cacho, T. Kim, K. Horiba, H. Kumigashira, T. Takahashi, Y. Ando, and T. Sato, Phys. Rev. Lett. **122**, 076402 (2019).
28 Z. Rao, H. Li, T. Zhang, S. Tian, C. Li, B. Fu, C. Tang, L. Wang, Z. Li, W. Fan, J. Li, Y. Huang, Z. Liu, Y. Long, C. Fang, H. Weng, Y. Shi, H. Lei, Y. Sun, T. Qian, and H. Ding, Nature **567**, 496 (2019).
29 D. S. Sanchez, I. Belopolski, T. A. Cochran, X. Xu, J. X. Yin, G. Chang, W. Xie, K. Manna, V. Süß, C. Y. Huang, N. Alidoust, D. Multer, S. S. Zhang, N. Shumiya, X. Wang, G. Q. Wang, T. R. Chang, C. Felser, S. Y. Xu, S. Jia, H. Lin, and M. Z. Hasan, Nature **567**, 500 (2019).
30 Y. Yang, H. Sun, J. Xia, H. Xue, Z. Gao, Y. Ge, D. Jia, S. Yuan, Y. Chong, and B. Zhang, Nat. Phys. **15**, 645 (2019).
31 N. B. M. Schröter, D. Pei, M. G. Vergniory, Y. Sun, K. Manna, F. de Juan, J. A. Krieger, V. Süß, M. Schmidt, P. Dudin, B. Bradlyn, T. K. Kim, T. Schmitt, C. Cacho, C. Felser, V. N. Strocov, and Y. Chen, Nat. Phys. **15**, 759 (2019).
32 A. C. Potter, I. Kimchi, and A. Vishwanath, Nat. Commun. **5**, 5161 (2014).
33 P. J. W. Moll, N. L. Nair, T. Helm, A. C. Potter, I. Kimchi, A. Vishwanath, and J. G. Analytis, Nature **535**, 266 (2016).
34 C. M. Wang, H. P. Sun, H. Z. Lu, and X. C. Xie, Phys. Rev. Lett. **119**, 136806 (2017).
35 C. Zhang, Y. Zhang, X. Yuan, S. Lu, J. Zhang, A. Narayan, Y. Liu, H. Zhang, Z. Ni, R. Liu, E. S. Choi, A. Suslov, S. Sanvito, L. Pi, H. Z. Lu, A. C. Potter, and F. Xiu, Nature **565**, 331 (2018).
36 H. He, C. Qiu, L. Ye, X. Cai, X. Fan, M. Ke, F. Zhang, and Z. Liu, Nature **560**, 61 (2018).
37 Z. Zhang, Y. Tian, Y. Wang, S. Gao, Y. Cheng, X. Liu, and J. Christensen, Adv. Mater. **30**, 1803229 (2018).
38 Z. Zhu, X. Huang, J. Lu, M. Yan, F. Li, W. Deng, and Z. Liu, Phys. Rev. Appl. **12**, 024007 (2019).
39 Z. G. Geng, Y. G. Peng, Y. X. Shen, Z. Ma, R. Yu, J. H. Gao, and X. F. Zhu, Phys. Rev. B **100**, 224105 (2019).
40 Y. G. Peng, Y. Li, Y. X. Shen, Z. G. Geng, J. Zhu, C. W. Qiu, and X. F. Zhu, Phys. Rev. Res. **1**, 033149 (2019).
41 H. Ge, X. Ni, Y. Tian, S. K. Gupta, M. H. Lu, X. Lin, W. D. Huang, C. T. Chan, and Y. F. Chen, Phys. Rev. Appl. **10**, 014017 (2018).
42 V. Peri, M. Serra-Garcia, R. Ilan, and S. D. Huber, Nat. Phys. **15**, 357 (2019).
43 R. A. Vicencio, C. Cantillano, L. Morales-Inostroza, B. Real, C. Mejía-Cortés, S. Weimann, A. Szameit, and M. I. Molina, Phys. Rev. Lett. **114**, 245503 (2015).
44 S. Mukherjee, A. Spracklen, D. Choudhury, N. Goldman, P. Öhberg, E. Andersson, and R. R. Thomson, Phys. Rev. Lett. **114**, 245504 (2015).
45 S. Taie, H. Ozawa, T. Ichinose, T. Nishio, S. Nakajima, and Y. Takahashi, Sci. Adv. **1**, e1500854 (2015).
46 Y. Li, T. Chen, X. Wang, Y. Xi, and Q. Liang, Phys. Lett. A **379**, 412 (2015).
47 D. Leykam, and S. Flach, APL Photon. **3**, 070901 (2018).
48 S. Longhi, Opt. Lett. **44**, 287 (2019).